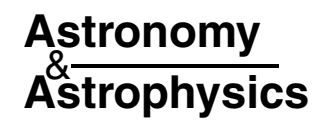
A&A 451, 273–284 (2006) DOI: 10.1051/0004-6361:20053846

© ESO 2006



A 3D radiative transfer framework

I. Non-local operator splitting and continuum scattering problems

P. H. Hauschildt¹ and E. Baron^{1,2,3}

- ¹ Hamburger Sternwarte, Gojenbergsweg 112, 21029 Hamburg, Germany e-mail: yeti@hs.uni-hamburg.de
- ² Homer L. Dodge Dept. of Physics and Astronomy, University of Oklahoma, 440 W. Brooks, Rm 100, Norman, OK 73019-2061, USA e-mail: baron@nhn.ou.edu
- ³ CRD, Lawrence Berkeley National Laboratory, MS 50F-1650, 1 Cyclotron Rd, Berkeley, CA 94720-8139, USA

Received 18 July 2005 / Accepted 3 January 2006

ABSTRACT

We describe a highly flexible framework to solve 3D radiation transfer problems in scattering dominated environments based on a long characteristics piece-wise parabolic formal solution and an operator splitting method. We find that the linear systems are efficiently solved with iterative solvers such as Gauss-Seidel and Jordan techniques. We use a sphere-in-a-box test model to compare the 3D results to 1D solutions in order to assess the accuracy of the method. We have implemented the method for static media, however, it can be used to solve problems in the Eulerian-frame for media with low velocity fields.

Key words. radiative transfer

1. Introduction

With the increase in computer power in the last few years, 3D hydrodynamical calculations are becoming increasingly common in astrophysics. Most hydrodynamical calculations treat radiation in a simplified manner, since a full solution of the 3D non-LTE radiative transfer problem is numerically much more expensive than the hydrodynamical calculation itself, which already stretch the limits of modern parallel computers. In many instances, such as the thermonuclear explosion of a white dwarf (thought to be the progenitor of type Ia supernova), the goal of the hydrodynamical simulations is to understand the mode of combustion and to handle the effects of turbulence in as realistic manner as possible and radiative transfer effects are ignored. However, in general since the ultimate validation or falsification of the results of sophisticated hydrodynamical modeling will be via comparison with the observed radiation from the astrophysical object being studied, and the radiation strongly affects the physical state of the matter in the atmosphere of the object (where the observed radiation originates) the effect of detailed radiative transfer effects cannot be ignored.

In many multi-dimensional hydrodynamics codes (for example ZEUS3D, Norman 2000), radiative transfer is treated in a simplified matter in order to determine the amount of energy transfered between the matter and radiation (the cooling function) although Dykema et al. (1996) presented a full

time-dependent 2D NLTE radiative transfer code, based on a variable Eddington factor method and equivalent two level atom formulation.

Recently Rijkhorst et al. (2005) presented a method of including 3D radiative transfer into modern 3D hydrodynamical codes (such as the ASCI FLASH code) but they only treated the solution of the radiative transfer equation in the absence of scattering, that is they their method only treats the formal solution of the radiative transfer equation and not the full self consistent scattering problem where the right hand side of the radiative transfer problem involves the radiation field itself. However, in astrophysical systems, the effect of scattering cannot be ignored and in fact it is due to scattering that the radiation field decouples from the local emission and absorption and the effects of the existence of the boundary are communicated globally over the atmosphere (Mihalas 1978). It is just this strong non-locality of the radiation field that makes the solution of the generalized radiative transfer problem so computationally demanding.

Steiner (1991) presented a 2D multi-grid method based on the short-characteristics method (Olson & Kunasz 1987; Olson et al. 1987) and showed that it worked in the case of a purely absorptive atmosphere, i.e., that the formal solution was tractable. Vath (1994) presented a 3D short characteristics method and showed that it had adequate scaling on a SIMD parallel architecture. In a series of papers 3D, short characteristics

methods for disk systems were presented by Adam (1990); Hummel (1994a,b); Hummel & Dachs (1992); Papkalla (1995). Our method is similar in spirit to these works, but we present a more detailed description of the construction of the approximate lambda operator (ALO), and the method of solution of the scattering problem.

Fabiani Bendicho et al. (1997) presented a multi-level, multi-grid, multi-dimensional radiative transfer scheme, using a lower triangular ALO and solving the scattering problem via a Gauss-Seidel method.

van Noort et al. (2002) presented a method of solving the full NLTE radiative transfer problem using the short characteristics method in 2D for Cartesian, spherical, and cylindrical geometry. They also used the technique of accelerated lambda iteration (ALI) (Olson et al. 1987; Olson & Kunasz 1987), however they restricted themselves to the case of a diagonal ALO. In addition they considered the case including velocity fields, but their method is feasible only in the case of a small velocity gradient across the atmosphere.

We describe below a simple framework to solve three dimensional (3D) radiation transport (RT) problems with a non-local operator splitting method. In subsequent papers we will extend this framework to solve 3D RT problems in relativistically moving configurations. Our method is similar to those described above, although we consider both short characteristics and long characteristics methods for the formal solution of the radiative transfer equation. We show that long-characteristics produce a significantly better numerical solution in our test cases for a strongly scattering dominated atmosphere. Short-characteristics are known to be diffusive and it is apparent in our numerical results. We also implement a partial parallelization of the method, although we defer a full discussion of the parallelization to future work.

2. Method

In the following discussion we use notation of Hauschildt (1992). First, we will describe the process for the formal solution, then we will describe how we construct the non-local approximate Λ operator, Λ^* , and methods to solve the necessary linear equations in the operator splitting step.

2.1. Framework

The 3D RT equations are easiest solved in a Cartesian coordinate system (e.g., Fabiani Bendicho et al. 1997), therefore we use a Cartesian grid of volume cells (voxels). Basically, the voxels are allowed to have different sizes but for the tests presented later in this paper we use fixed size voxels (as the simplest option). The values of physical quantities, such as temperatures, opacities and mean intensities, are averages over a voxel, which, therefore, also fixes the local physical resolution of the grid. In the following we will specify the size of the voxel grid by the number of voxels along each positive axis, e.g., $n_x = n_y = n_z = 32$ specifies a voxel grid from voxel coordinates (-32, -32, -32) to (32, 32, 32) for a total of $(2*32+1)^3 = 274625$ voxels, 65 along each axis. The voxel (0,0,0) is at the center of the voxel grid. The voxel centers are

the grid points. The voxel coordinates are related by grid scaling factors to physical space, depending on the problem. The framework does not require $n_x = n_y = n_z$, we use this for the tests presented in this paper for convenience.

The applications that we intend to solve with the 3DRT framework will involve optically thick environments with a significant scattering contribution, e.g., modeling the light reflected by an extrasolar giant planet close to its parent star. Therefore, not only a formal solution is required but the full solution of the 3D radiative transfer equation with scattering. In this paper, we describe a method based on the operator splitting approach. Operator splitting works best if a non-local Λ^* operator is used in the calculations (e.g., Hauschildt et al. 1994), therefore we describe a non-local Λ^* method here. The operator splitting method can be combined with other methods, like multigrids, to allow for greater flexibility and better convergence, which we will discuss in a later paper.

2.2. Radiative transfer equation

The static radiative transfer equation in 3D may be written

$$\hat{\boldsymbol{n}} \cdot \nabla I(\boldsymbol{v}, \boldsymbol{x}, \hat{\boldsymbol{n}}) = \eta(\boldsymbol{v}, \boldsymbol{x}) - \chi(\boldsymbol{v}, \boldsymbol{x})I(\boldsymbol{v}, \boldsymbol{x}, \hat{\boldsymbol{n}}) \tag{1}$$

where $I(v, x, \hat{n})$ is the specific intensity at frequency v, position x, in the direction \hat{n} , $\eta(v, x)$ is the emissivity at frequency v and position x, and $\chi(v, x)$ is the total extinction at frequency v and position x. The source function $S = \eta/\chi$. Here, we will work in the steady-state so that $\partial I/\partial t = 0$, and in Cartesian coordinates so the $\nabla = \frac{\partial}{\partial x} + \frac{\partial}{\partial y} + \frac{\partial}{\partial z}$ and the direction \hat{n} is defined by two angles (θ, ϕ) at the position x.

2.3. The operator splitting method

The mean intensity J is obtained from the source function S by a formal solution of the RTE which is symbolically written using the Λ -operator Λ as

$$J = \Lambda S. \tag{2}$$

The source function is given by $S = (1 - \epsilon)J + \epsilon B$, where ϵ denotes the thermal coupling parameter and B is Planck's function.

The Λ -iteration method, i.e. to solve Eq. (2) by a fixed-point iteration scheme of the form

$$J_{\text{new}} = \Lambda S_{\text{old}}, \quad S_{\text{new}} = (1 - \epsilon)J_{\text{new}} + \epsilon B,$$
 (3)

fails in the case of large optical depths and small ϵ . Here, S_{old} is the current estimate for the source function S and S_{new} is new, improved, extimate of S for the next iteration. The failure to converge of the Λ -iteration is caused by the fact that the largest eigenvalue of the amplification matrix is approximately (Mihalas et al. 1975) $\lambda_{\text{max}} \approx (1 - \epsilon)(1 - T^{-1})$, where T is the optical thickness of the medium. For small ϵ and large T, this is very close to unity and, therefore, the convergence rate of the Λ -iteration is very poor. A physical description of this effect can be found in Mihalas (1980).

The idea of the ALI or operator splitting (OS) method is to reduce the eigenvalues of the amplification matrix in the iteration scheme (Cannon 1973) by introducing an approximate Λ -operator (ALO) Λ^* and to split Λ according to

$$\Lambda = \Lambda^* + (\Lambda - \Lambda^*) \tag{4}$$

and rewrite Eq. (3) as

$$J_{\text{new}} = \Lambda^* S_{\text{new}} + (\Lambda - \Lambda^*) S_{\text{old}}.$$
 (5)

This relation can be written as Hamann (1987)

$$[1 - \Lambda^*(1 - \epsilon)] J_{\text{new}} = J_{\text{fs}} - \Lambda^*(1 - \epsilon) J_{\text{old}}, \tag{6}$$

where $J_{\rm fs} = \Lambda S_{\rm old}$ and $J_{\rm old}$ is the current estimate of the mean intensity J. Equation 6 is solved to get the new values of J which is then used to compute the new source function for the next iteration cycle.

Mathematically, the OS method belongs to the same family of iterative methods as the Jacobi or the Gauss-Seidel methods (Golub & Van Loan 1989). These methods have the general form

$$Mx^{k+1} = Nx^k + b (7)$$

for the iterative solution of a linear system Ax = b where the system matrix A is split according to A = M - N. In the case of the OS method we have $M = 1 - \Lambda^*(1 - \epsilon)$ and, accordingly, $N = (\Lambda - \Lambda^*)(1 - \epsilon)$ for the system matrix $A = 1 - \Lambda(1 - \epsilon)$. The convergence of the iterations depends on the spectral radius, $\rho(G)$, of the iteration matrix $G = M^{-1}N$. For convergence the condition $\rho(G) < 1$ must be fulfilled, this puts a restriction on the choice of Λ^* . In general, the iterations will converge faster for a smaller spectral radius. To achieve a significant improvement compared to the Λ -iteration, the operator Λ^* is constructed so that the eigenvalues of the iteration matrix G are much smaller than unity, resulting in swift convergence. Using parts of the exact Λ matrix (e.g., its diagonal or a tri-diagonal form) will optimally reduce the eigenvalues of the G. The calculation and the structure of Λ^* should be simple in order to make the construction of the linear system in Eq. (6) fast. For example, the choice $\Lambda^* = \Lambda$ is best in view of the convergence rate (it is equivalent to a direct solution by matrix inversion) but the explicit construction of Λ is more time consuming than the construction of a simpler Λ^* . The solution of the system Eq. (6) in terms of linear algebra, using modern linear algebra packages such as, e.g., LAPACK (Anderson et al. 1992), is so fast that its CPU time can be neglected for the small number of variables encountered in 1D problems (typically the number of discrete shells is about 50). However, for 2D or 3D problems the size of Λ gets very large due to the much larger number of grid points as compared to the 1D case. Matrix inversions, which are necessary to solve Eq. (6) directly, therefore become extremely time consuming. This makes the direct solution of Eq. (6) more CPU intensive even for Λ^* 's of moderate bandwidth, except for the trivial case of a diagonal Λ^* . Different methods like modified conjugate gradient methods (Turek 1993) may be effective for these 2D or 3D problems.

The CPU time required for the solution of the RTE using the OS method depends on several factors: (a) the time required

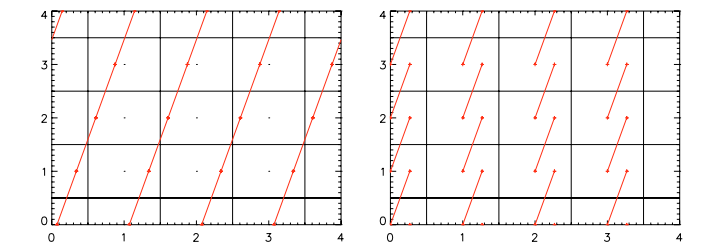


Fig. 1. Schematic sketch of the different types of characteristics used in the framework. The left panel shows the long characteristics, the right panel the short characteristics. The voxel boundaries and centers ("+" symbols) are indicated. The "+" denote the points between which the geometric distance is used to compute optical depth steps.

for a formal solution and the computation of $J_{\rm fs}$, (b) the time needed to construct Λ^* , (c) the time required for the solution of Eq. (6), and (d) the number of iterations required for convergence to the prescribed accuracy. Points (a), (b) and (c) depend mostly on the number of spatial points, and can be assumed to be fixed for any given configuration. However, the number of iterations required to convergence depends strongly on the bandwidth of Λ^* . This indicates, that there is an *optimum bandwidth* of the Λ^* -operator which will result in the shortest possible CPU time needed for the solution of the RTE, see Hauschildt et al. (1994).

2.4. Formal solution

The formal solution through the voxel grid can be performed by a variety of methods. So far, we have implemented both a short-characteristic (SC, Olson et al. 1987) and a longcharacteristic (LC) method. Long and short characteristics are shown schematically in Fig. 1. In our current implementation, the long characteristics are followed continuously through the voxel grid, the short characteristics start at the center of a voxel and step closest to the center of the next voxel. The distances along a (short or long) characteristic are then used to compute the optical depth steps. Along a characteristic (either short or long), the formal solution is computed using a piecewise parabolic (PPM) or piece-wise linear (PLM) interpolation and integration of the source function (Olson & Kunasz 1987). Auer (2003) discusses the effect that high order interpolation may cause problems, therefore, we automatically use piece-wise linear interpolation if the change in the source function along the 3 points of the PPM step would be larger than a prescribed threshold (typically factors of 100) or if the optical depth along the characteristic is very small (typically less than 10^{-3}). Depending on the direction (θ, ϕ) of the characteristic, the formal solution proceeds through the voxel grid.

Therefore, *along a characteristic* [which is in the static case just a straight line with given (θ, ϕ)] the transport equation is simply

$$\frac{\mathrm{d}I}{\mathrm{d}\tau} = I - S. \tag{8}$$

With this definition, the formal solution of the RTE along the characteristics can be written in the following way (cf. Olson & Kunasz 1987, for a derivation of the formulae) where we have

suppressed the index labeling the characteristic; τ_i denotes the optical depth along the characteristic with $\tau_1 \equiv 0$ and $\tau_{i-1} \leq \tau_i$ while τ is calculated using piecewise linear interpolation of χ along the characteristic, viz.

$$I(\tau_i) = I(\tau_{i-1}) \exp(\tau_{i-1} - \tau_i)$$

+
$$\int_{-\tau_i}^{\tau_i} S(\tau) \exp(\tau - \tau_i) d\tau$$

$$I(\tau_i) \equiv I_{i-1} \exp(-\Delta \tau_{i-1}) + \Delta I_i \tag{10}$$

i labels the points along a characteristic and $\Delta \tau_i$ is calculated using piecewise linear interpolation of χ along the characteristic

$$\Delta \tau_{i-1} = (\chi_{i-1} + \chi_i)|s_{i-1} - s_i|/2. \tag{11}$$

The starting points of each characteristic are at the center of the voxels on their starting faces of the voxel grid.

The source function $S(\tau)$ along a characteristic is interpolated by linear or parabolic polynomials so that

$$\Delta I_i = \alpha_i S_{i-1} + \beta_i S_i + \gamma_i S_{i+1} \tag{12}$$

with

$$\alpha_i = e_{0i} + [e_{2i} - (\Delta \tau_i + 2\Delta \tau_{i-1})e_{1i}]/[\Delta \tau_{i-1}(\Delta \tau_i + \Delta \tau_{i-1})]$$
 (13)

$$\beta_i = \left[(\Delta \tau_i + \Delta \tau_{i-1}) e_{1i} - e_{2i} \right] / \left[\Delta \tau_{i-1} \Delta \tau_i \right]$$
(14)

$$\gamma_i = [e_{2i} - \Delta \tau_{i-1} e_{1i}] / [\Delta \tau_i (\Delta \tau_i + \Delta \tau_{i-1})]$$
(15)

for parabolic interpolation and

$$\alpha_i = e_{0i} - e_{1i}/\Delta \tau_{i-1} \tag{16}$$

$$\beta_i = e_{1i}/\Delta \tau_{i-1} \tag{17}$$

$$\gamma_i = 0 \tag{18}$$

for linear interpolation. The auxiliary functions are given by

$$e_{0i} = 1 - \exp(-\Delta \tau_{i-1}) \tag{19}$$

$$e_{1i} = \Delta \tau_{i-1} - e_{0i} \tag{20}$$

$$e_{2i} = (\Delta \tau_{i-1})^2 - 2e_{1i} \tag{21}$$

and $\Delta \tau_i \equiv \tau_{i+1} - \tau_i$ is the optical depth along the characteristic from point i to point i+1. The linear coefficients have to be used (at least) at the last integration point along each characteristic, and for some cases it might be better to also use linear interpolation for some inner points so as to ensure stability.

The integration over solid angle can be done in the static case using a simple Simpson or trapezoidal quadrature formula. However, in the case of Lagrangian frame radiation transport, the angles (θ, ϕ) vary along a (curved) characteristic. Therefore, the (θ, ϕ) grid changes for each voxel and developing a quadrature formula in advance requires a pass through all voxels, storing all (θ, ϕ) points for each of them. For larger grids this will amount to substantial long term memory requirements as the resulting quadrature weights will have to be stored for each

 (θ, ϕ) pair at all voxels. To avoid this, we have implemented a simple Monte-Carlo (MC) scheme to perform the integration over solid angle. In the MC integration, the integral

$$J = \frac{1}{4\pi} \int_0^{2\pi} \int_0^{\pi} I \sin\theta \, d\theta d\phi$$

is replaced by a simple MC sum of the form

(10)
$$J \approx \frac{1}{2\pi^2} \sum I \sin \theta$$

where the sum goes over all solid angle points (θ, ϕ) . The (θ, ϕ) are randomly selected and given equal weight in the MC sums. This also works for precribed (θ, ϕ) grids as long as the number of (θ, ϕ) points is sufficiently large. The accuracy is improved by maintaining the normalization numerically for a unity valued test function. The MC method has the advantage that the solid angle points can vary from voxel to voxel (important for configurations with velocity fields where the transfer equation is solved in the locally co-moving frame). In the static case, the accuracy of the MC method is only insignificantly worse than that of the deterministic quadrature, which indicates that the MC integration will be very useful in the case of 3D radiation transport in moving media.

2.4.1. Computation of Λ^*

As demonstrated by Olson et al. (1987) and Olson & Kunasz (1987), the coefficients α , β , and γ can be used to construct diagonal and tri-diagonal Λ^* operators for 1D radiation transport problems. In fact, up to the full Λ matrix can be constructed by a straightforward extension of the idea (Hauschildt et al. 1994; Hauschildt & Baron 2004). These non-local Λ^* operators not only lead to excellent convergence rates but they also avoid the problem of false convergence that is inherent in the Λ iteration method and can also be an issue for diagonal (purely local) Λ^* operators. Therefore, it is highly desirable to implement a non-local Λ^* also for the 3D case. The tri-diagonal operator in the 1D case is simply a nearest neighbor Λ^* that considers the interaction of a point with its two direct neighbors. In the 3D case, the nearest neighbor Λ^* considers the interaction of a voxel with the (up to) $3^3 - 1 = 26$ surrounding voxels (this definition considers a somewhat larger range of voxels that a strictly face-centered view of just 6 nearest neighbors). This means that the non-local Λ^* requires the storage of 27 (26 surrounding voxels plus local, i.e., diagonal effects) times the total number of voxels Λ^* elements. This can be reduced, for example if one considers only the voxels that share a face to a total of 7 elements for each voxel. However, this would ignore the effect of characteristics that pass "diagonally" through a voxel and would therefore lead to a slower convergence rate.

The construction of the Λ^* operator proceeds in the same way as discussed in Hauschildt (1992). In the 3D case, the "previous" and "next" voxels along each characteristic must be known so that the contributions can be attributed to the correct voxel. Therefore, we use a data structure that attaches to each voxel its effects on its neighbors. The scheme can be extended trivially to include longer range interactions for better

convergence rates (in particular on larger voxel grids), however the memory requirements to simply store Λ^* ultimately scales like n^3 where n is the total number of voxels. The storage requirements can be reduced by, e.g., using Λ^* 's of different widths for different voxels. Storage requirements are not so much a problem if a domain decomposition parallelization method is used and enough processors are available. Below we will show some results for test cases with larger operators.

We describe here the general procedure of calculating the Λ^* with *arbitrary* bandwidth, up to the full Λ -operator, for the method in spherical symmetry (Hauschildt et al. 1994). The construction of the Λ^* is described in Olson & Kunasz (1987), so that we here summarize the relevant formulae. In the method of Olson & Kunasz (1987), the elements of the row of Λ^* are computed by setting the incident intensities (boundary conditions) to zero and setting $S(i_x, i_y, i_z) = 1$ for one voxel (i_x, i_y, i_z) and performing a formal solution analytically.

We describe the construction of Λ^* using the example of a single characteristic. The contributions to the Λ^* at a voxel j are given by

$$\Lambda_{i,j} = 0 \quad \text{for } i < j - 1 \tag{22}$$

$$\Lambda_{i-1,j} = \gamma_{i-1} \quad \text{for } i = j-1 \tag{23}$$

$$\Lambda_{i,j} = \Lambda_{i-1,j} \exp(-\Delta \tau_{i-1}) + \beta_i^k \quad \text{for } i = j$$
 (24)

$$\Lambda_{i+1,j} = \Lambda_{i,j} \exp(-\Delta \tau_i) + \alpha_{i+1} \quad \text{for } i = j+1$$
 (25)

$$\Lambda_{i,j} = \Lambda_{i-1,j} \exp\left(-\Delta \tau_{i-1}\right) \text{for } j+1 < i.$$
(26)

These contributions are computed along a characteristic, here i labels the voxels *along* the characteristic under consideration. These contributions are integrated over solid angle with the same method (either deterministic or through the Monte-Carlo integration) that is used for the computation of the J. For a nearest neighbor Λ^* , the process of Eq. (26) is stopped with i=j+1, otherwise it is continued until the required bandwidth has been reached (or the characteristic has reached an outermost voxel and terminates).

2.5. Operator splitting step

For a diagonal Λ^* the solution of Eq. (6) is just a division by $[1 - \Lambda^*(1 - \epsilon)]$ which requires very little effort. For the nonlocal Λ^* operator, a matrix equation has to be solved at each step in order to compute J_{new} . For the nearest neighbor operator the matrix structure is that of a sparse band matrix where the bandwidth of the matrix is proportional to the square of the maximum number of points along a coordinate and there are a total of 27 non-zero entries in every column of the matrix. This system can be solved by any suitable method. For example, we have implemented a solver based on LAPACK (Anderson et al. 1992) routines. Although this solver works fine for small grids $[(2*16+1)^3]$ voxels with a bandwidth of 1123, the memory requirements rise beyond available single-CPU limits with already only $(2 * 32 + 1)^3$ voxels with a bandwidth of 4291. For a more realistic grid of $(2 * 256 + 1)^3$ voxels the bandwidth is more than 250000. Therefore, a standard band matrix solver is only useful for comparison and testing on very small grids.

Other sparse matrix solvers (for example, Xiaoye & Demmel 2003) have similar memory scaling properties.

As an alternative to direct solutions of Eq. (6) we have implemented iterative solvers. These solvers have the huge advantage that their memory requirements are minimal to modest. In addition, they can be tailored to the special format of the matrix in Eq. (6) which makes coding the methods very simple. We obtained extremely good results with the Jordan and the Gauss-Seidel methods, which converge rapidly to a relative accuracy of 10⁻¹⁰. For either method, Ng acceleration turned out to be very useful, reducing the number of iterations significantly. In addition, the Rapido method (Zurmühl & Falk 1986) which was constructed to solve systems of the form

$$(1 - M)x = a \tag{27}$$

can be used. However, Rapido has strong constraints on the spectral radius of M and this cannot be used for problems that involve substantial scattering. In the test calculations discussed below we have used the Jordan or Gauss-Seidel solvers as they are the fastest of the solvers we have implemented. We verified that all solvers give the same results.

3. Application examples

As a first step we have implemented the method as a MPI parallelized Fortran 95 program. The parallelization of the formal solution is presently implemented over solid angle space as this is the simplest parallelization option and also one of the most efficient (a domain decomposition parallelization method will be discussed in a subsequent paper). In addition, the Jordan solver of the Operator splitting equations is parallelized with MPI (see below for scaling properties of the MPI implementation). The number of parallelization related statements in the code is small, about 320 out of a total of about 7900.

Our basic continuum scattering test problem is similar to that discussed in Hauschildt (1992) and in Hauschildt & Baron (2004). This test problem covers a large dynamic range of about 9 dex in the opacities and overall optical depth steps along the characteristics and, in our experience, constitutes a reasonably challenging setup for the radiative transfer code. The application of the 3D code to "real" problems is in preparation and requires a substantial amount of development work (in progress). For the 1D code we have found that the test case is actually pretty much a worst case scenario and that it generally works better in real world problems. We use a sphere with a grey continuum opacity parameterized by a power law in the continuum optical depth $\tau_{\rm std}$. The basic model parameters are

- 1. Inner radius $r_{\rm c}=10^{13}\,{\rm cm},$ outer radius $r_{\rm out}=1.01\times 10^{15}\,{\rm cm}.$
- 2. Minimum optical depth in the continuum $\tau_{\rm std}^{\rm min}=10^{-4}$ and maximum optical depth in the continuum $\tau_{\rm std}^{\rm max}=10^4$.
- 3. Grey temperature structure with $T_{\text{eff}} = 10^4 \text{ K}$.
- 4. Outer boundary condition $I_{bc}^- \equiv 0$ and diffusion inner boundary condition for all wavelengths.
- 5. Continuum extinction $\chi_c = C/r^2$, with the constant C fixed by the radius and optical depth grids.

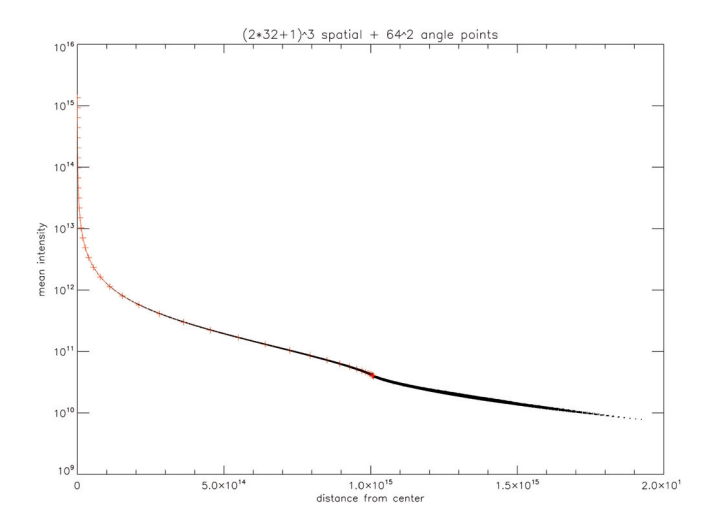


Fig. 2. Comparison of the results obtained for the LTE test with the 1D solver (+ symbols) and the 3D solver. The *x* axis shows the distances from the center of the sphere, the *y* axis the log of the mean intensity.

6. Parameterized coherent & isotropic continuum scattering by defining

$$\chi_{\rm c} = \epsilon_{\rm c} \kappa_{\rm c} + (1 - \epsilon_{\rm c}) \sigma_{\rm c} \tag{28}$$

with $0 \le \epsilon_c \le 1$. κ_c and σ_c are the continuum absorption and scattering coefficients.

The test model is just an optically thick sphere put into the 3D grid. This problem is used because the results can be directly compared with the results obtained with our 1D spherical radiation transport code (Hauschildt 1992) to assess the accuracy of the method. The sphere is centered at the center of the Cartesian grid, which is in each axis 10% larger than the radius of the sphere. For the test calculations we use voxel grids with the same number of spatial points in each direction (see below). The solid angle space was discretized in (θ, ϕ) with $n_{\theta} = n_{\phi}$ if not stated otherwise. In the following we discuss the results of various tests. In all tests we use the LC method for the 3D RT solution unless stated otherwise.

3.1. LTE tests

In this test we have set $\epsilon = 1$ to test the accuracy of the formal solution by comparing to the results of the 1D code. The 1D solver uses 50 radial points, distributed logarithmically in optical depth. For the 3D solver we tested "small" grids with $n_x = n_y = n_z = 2 * 32 + 1$ points along each axis, for a total of $65^3 \approx 2.7 \times 10^5$ voxels, as well as "medium" $(n_x = n_y = n_z = 2 * 64 + 1 \text{ with a total of } 129^3 \approx 2.1 \times 10^6 \text{ vox-}$ els) and "large" $(n_x = n_y = n_z = 2 * 96 + 1)$ with a total of $193^3 \approx 7.2 \times 10^6$ voxels). The large grid was limited by available memory for the storage of the non-local Λ^{\ast} operator. The solid angle space discretization uses, in general, $n_{\theta} = n_{\phi} =$ 64 points. In Fig. 2 we show the mean intensities as function of distance from the center for both the 1D (+ symbols) and the 3D solver. The results show excellent agreement between the two solutions, thus the 3D RT formal solution is comparable in accuracy with the 1D formal solution. We demonstrate

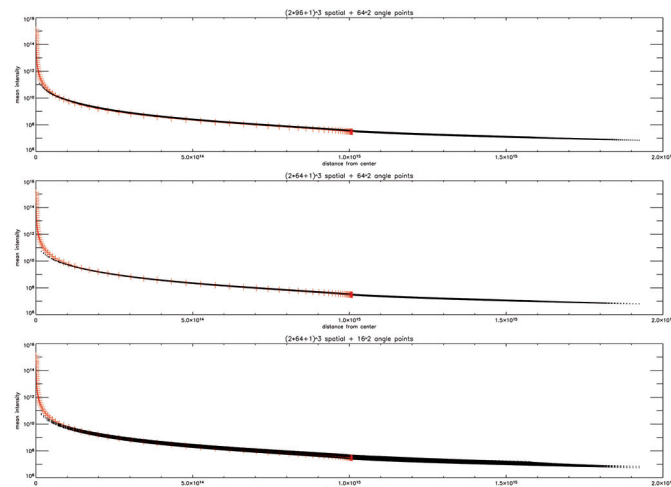


Fig. 3. Comparison of the results obtained for the scattering dominated ($\epsilon = 10^{-4}$) test with the 1D solver (+ symbols) and the 3D solver. The *x* axis shows the distances from the center of the sphere, the *y* axis the log of the mean intensity. The top panel shows the results for a (spatial; solid angle) grid with (193³; 64²) points, the middle panel for (129³; 64²) points and the bottom panel for (129³; 16²) points.

below that for the conditions used in these tests a larger number of solid angle points significantly improves the accuracy of the mean intensities.

3.2. Tests with continuum scattering

3.2.1.
$$\epsilon = 10^{-4}$$

For this test, we use the same basic structure setup as for the LTE test, however we now use $\epsilon = 10^{-4}$ for a scattering dominated atmosphere. The comparison with the results obtained with the 1D RT code (with 100 radial points) are compared to the 3D RT code results in Fig. 3. Note the factor of about 1000 difference between the solution for $\epsilon = 10^{-4}$ and the results of the formal solution with S = B shown in Fig. 2 at the largest distances (the iterations were started with S = B). Figure 3 shows the results for the "large" and "medium" spatial grids and for 2 different solid angle discretizations (64² and 16² solid angle points). For both the 1D and the 3D code the mean intensities were iterated to a relative accuracy of 10^{-8} (see below for details on convergence rates). The graph highlights the need for a rather fine solid angle grid for the test problem. With a small number of angular points (bottom panel in Fig. 3) the numerically induced spread of the mean intensities is significantly larger than with a 42 finer angular grid (shown in the middle panel). A change in spatial grid resolution has a much smaller effect on the results than the number of solid angle points as shown in the top two panels of Fig. 3. The spatial resolution of the "small" grid is, however, too coarse to represent the test problem, in particular in the inner parts of the structure.

The importance of the angular resolution is also demonstrated in Fig. 4 which shows the contours of the mean intensity on the six "faces" of the voxel cube for 129^3 spatial points and 16^2 (left panel) and 64^2 (right panel) solid angles.

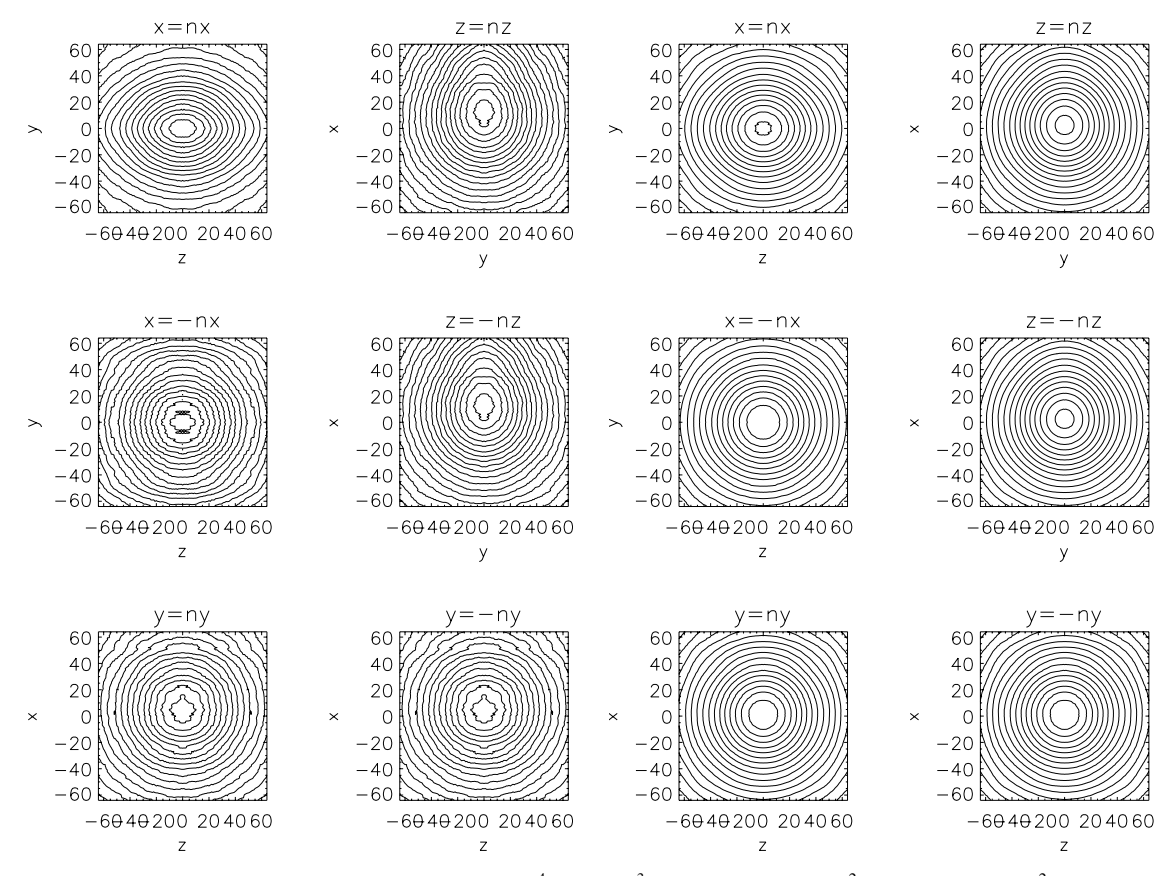


Fig. 4. Mean intensity contour plots for the test case with $\epsilon = 10^{-4}$ with 129^3 spatial points and 16^2 (*left panel*) and 64^2 solid angle points. The axes are labeled by voxel index with (x, y, z) = (0, 0, 0) being the center of the voxel grid. Each plot shows one outside face of the voxel cube (the physical scales are the same in all directions).

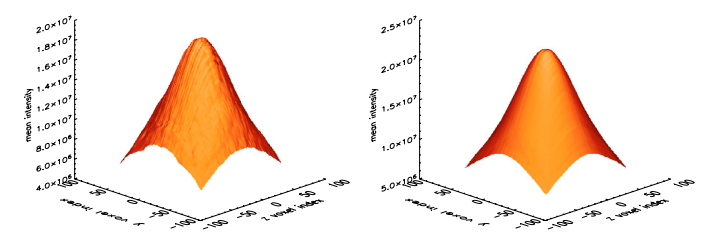


Fig. 5. Mean intensity surfaces at the z - y face for the test case with $\epsilon = 10^{-4}$, 129^3 spatial points, and 16^2 (*left panel*) and 64^2 solid angle points. The axes are labeled by voxel index with (x, y, z) = (0, 0, 0) being the center of the voxel grid. Each plot shows one outside face of the voxel cube (the physical scales are the same in all directions).

The calculation with 64^2 solid angle points shows symmetric contours whereas the smaller 16^2 angle points model shows asymmetries and 'banding' like structures on all faces (in particular on the x-y faces). This clearly indicates that for the test conditions used the angular resolution has to be larger than 16^2 for accurate solutions. This can also be seen in surface plots of the mean intensities at the $-n_x$ faces of the z-y planes for both calculations, cf. Fig. 5. The surface calculated with 64^2 angles is much smoother and shows no or little banding compared to the surface for 16^2 angular points. The effects of higher spatial resolution on the J surface at the z-y face is shown in Fig. 6. Clearly, 64^2 angles produce a smooth surface without significant artifacts for the test case.

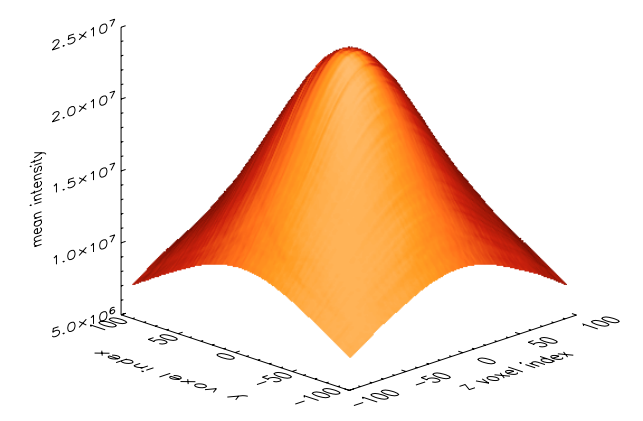


Fig. 6. Mean intensity surface at the z - y face for the test case with $\epsilon = 10^{-4}$ with 193^3 spatial points and 64^2 solid angle points. The axes are labeled by voxel index with (x, y, z) = (0, 0, 0) being the center of the voxel grid.

The convergence properties of the various methods for this test case are shown in Fig. 7. As expected, the Λ iteration converges very slowly and requires more than 300 iterations to reach a relative error of less than 10^{-8} . The diagonal Λ^* operator converges significantly better than the Λ iteration but is still rather slowly convergent. The nearest neighbor Λ^* converges substantially faster (by more than a factor of 3 than the diagonal Λ^*). The diagonal and nearest neighbor iterations can be accelerated by using Ng's method (Ng 1974), as shown in

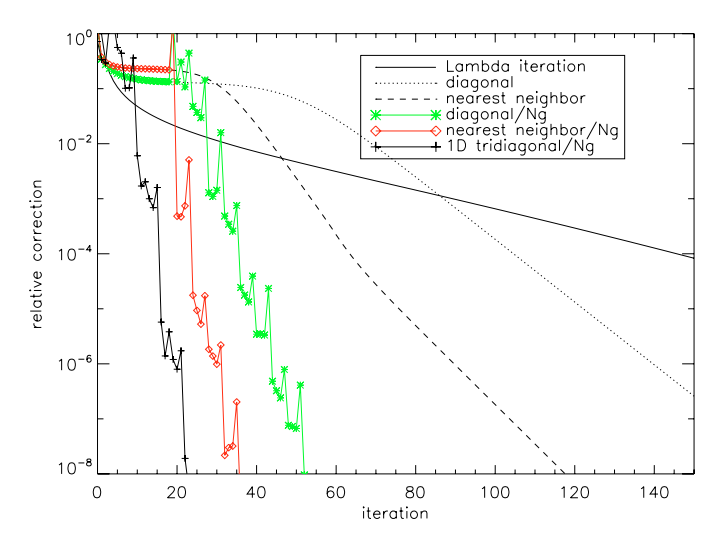


Fig. 7. Convergence properties of the codes for the $\epsilon = 10^{-4}$ test case. The labels indicate the different methods used. The 3D test runs use 65^3 spatial and 16^2 angular points.

Fig. 7. In both cases, a 4th order Ng acceleration was used after 20 initial iterations, starting Ng acceleration too early can lead to convergence failures since Ng acceleration is based on extrapolation. An attempt to apply the Ng acceleration to the Λ iteration was not successful, similar to the 1D case, as the convergence rate of the Λ iteration appears to be too small to be useful for the Ng method. For comparison, we show in Fig. 7 the convergence properties of the 1D RT solver with a tridiagonal Λ^* and Ng acceleration (here started much earlier). The convergence rates of the 1D tri-diagonal and 3D nearest neighbor methods are very comparable. The convergence properties are also relevant for the overall speed of the method: whereas the time for the formal solution (for a given number of voxels and processors) depends roughly linearly on the total number of solid angle points, the time for the solution of the operator splitting step does not depend on the number of angle points and actually decreases with iteration number if the Jordan, Gauss-Seidel or Rapido solvers are used. Therefore, the nearest neighbor operator will become more and more efficient as the number of angles and/or voxels increases.

The smaller initial corrections of the Λ iteration are actually an indication that it just corrects too little, the operator splitting method gives initially much larger corrections. This is exactly like similar test cases in 1D that we have tried. The initial corrections are so large because the initial guesses are very wrong (intentionally) so that between initial guess and final result we have changes by close to 10 orders of magnitude. This means that the initial corrections of the operator splitting method have to be large.

The convergence rates will depend on the grid resolution as the optical depths between voxels will be smaller for larger resolutions and thus the coupling between voxels will be stronger. This effect is shown in Fig. 8 where we show the convergence rates for various grids. The convergence rates are independent of the number of solid angle points but depend weakly on the number of grid points, as expected. Thus, for voxel grids with

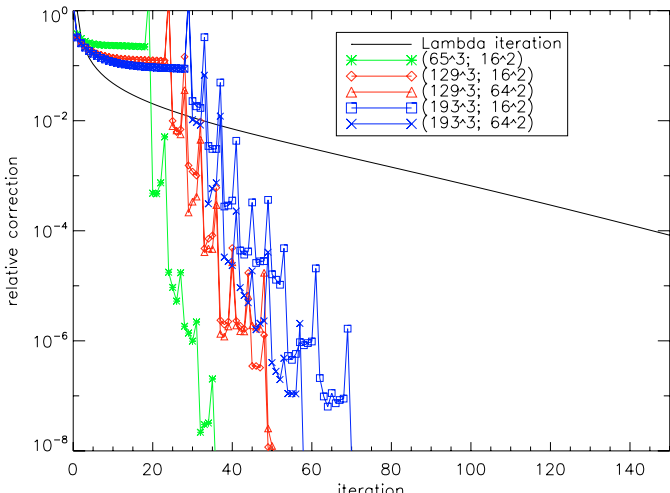


Fig. 8. Convergence properties of the codes for the $\epsilon = 10^{-4}$ test case and different grid sizes. The labels indicate the different grid sizes used, all but the Λ iteration use the nearest neighbor operator with Ng acceleration.

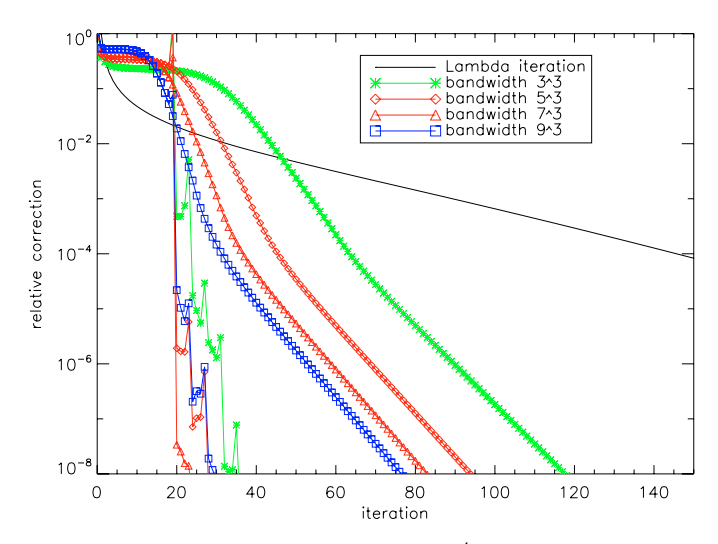


Fig. 9. Convergence properties of the $\epsilon = 10^{-4}$ test case for various Λ^* operator bandwidth choices with and without Ng acceleration.

higher resolution, a larger Λ^* (more neighbors) will be more useful than for coarser voxel grids.

Figure 9 shows the convergence rates for the $\epsilon=10^{-4}$ test case for different Λ^* bandwidths. The wider Λ^* 's lead to improved convergence rates; however, the net wallclock time increases for the wider Λ^* 's in the parallel code. This is caused by the substantially larger amount of information that needs to be passed between processes in order to build the wider Λ^* . In addition, the memory requirements for a *given* number of voxels scales like the cube of the number of neighbors considered in the Λ^* . As Fig. 9 demonstrates, the convergence is strongly improved by the use of Ng acceleration, however, for larger Λ^* 's the Ng method can be detrimental for wider Λ^* compared to narrower Λ^* .

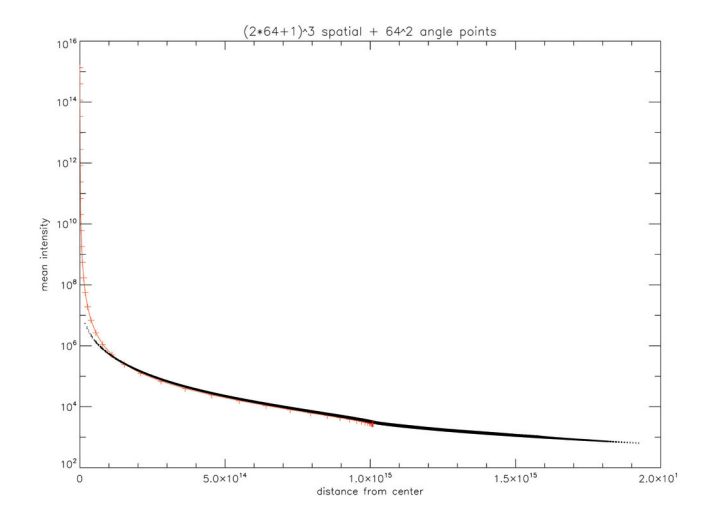


Fig. 10. Comparison of the results obtained for the scattering dominated ($\epsilon = 10^{-8}$) test with the 1D solver (+ symbols) and the 3D solver. The *x* axis shows the distances from the center of the sphere, the *y* axis the log of the mean intensity. The graph shows the results for a (spatial; solid angle) grid with $(129^3; 64^2)$ points. Note the large dynamic range (12 dex) of the mean intensities.

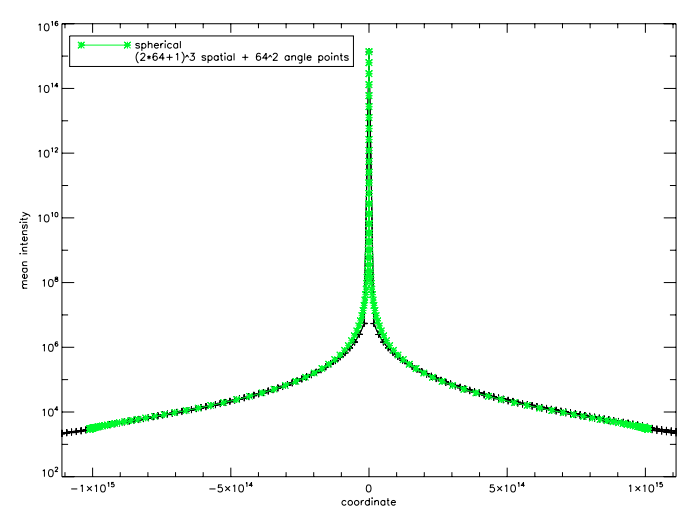


Fig. 11. Comparison of the results obtained for the scattering dominated ($\epsilon = 10^{-8}$) test with the 1D solver (+ symbols) and the 3D solver for slices along the x, y, and z axes. The plot shows the results for a (spatial; solid angle) grid with $(129^3; 64^2)$ points. Note the large dynamic range (12 dex) of the mean intensities.

3.2.2. $\epsilon = 10^{-8}$

The final test we present in this paper considers a case with a much larger scattering contribution: $\epsilon=10^{-8}$. The results for a grid with 129^3 voxels and 64^2 angular points are shown in Fig. 10. Figure 11 shows the results for slices along the coordinate axes (the two coordinates being centered, respectively). Even though the dynamic range of the mean intensities is huge, nearly 12 dex, the results are quite accurate. For this case the lack of spatial resolution in the inner parts of the voxel grid can be seen. Here $|\nabla J|$ is huge and cannot be fully resolved by the 3D RT code (the 1D code naturally has much higher resolution). However, only a few voxels away from the center the results agree very well.

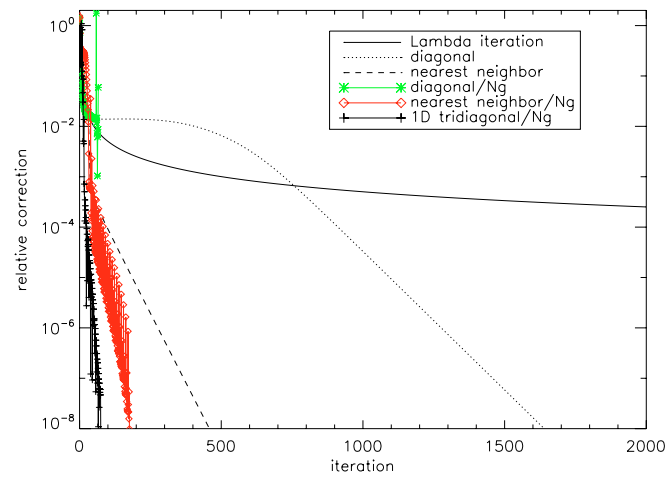


Fig. 12. Convergence properties of the codes for the $\epsilon = 10^{-8}$ test case. The labels indicate the different methods used. These test runs use 65^3 spatial and 16^2 angular points.

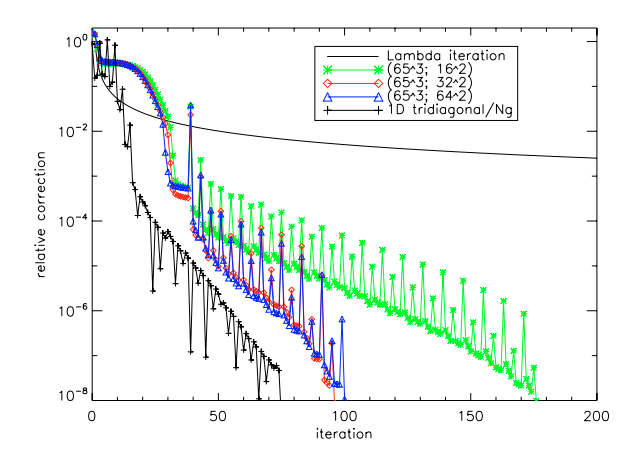


Fig. 13. Convergence properties of the codes for the $\epsilon=10^{-8}$ test case and different angular grid sizes. The labels indicate the different grid sizes used, all but the Λ iteration use the nearest neighbor operator with Ng acceleration.

The convergence plots in Fig. 12 show the results for a very difficult test case with $\tau_{\rm std}^{\rm max}=10^8$ for a fixed voxel and solid angle grid with 65^3 voxels and 16^2 angular points. For this test, the Λ iteration fails completely. The diagonal operator provides significant speed-up, but still requires more than 1600 iterations to reach the required convergence limit. For this test, the Ng acceleration does not work with the diagonal operator, the iteration process failed immediately after it was started. It is likely that a better result could be obtained if Ng acceleration is started in the steep part of the diagonal operator's convergence, e.g., after about 500 regular iterations. The nearest neighbor operator leads to much faster convergence, even without Ng acceleration the solution converges in about 450 iterations. Here, Ng acceleration works very well with the nearest neighbor operator, convergence is reached after 177 iterations. This is still about a factor of 2 more than for the 1D code, but much better than with the diagonal operator. The variation of the convergence rate for the nearest neighbor operator and Ng acceleration with the size of the solid angle grid is shown in Fig. 13. The case with the smallest angular grid (16² points) actually

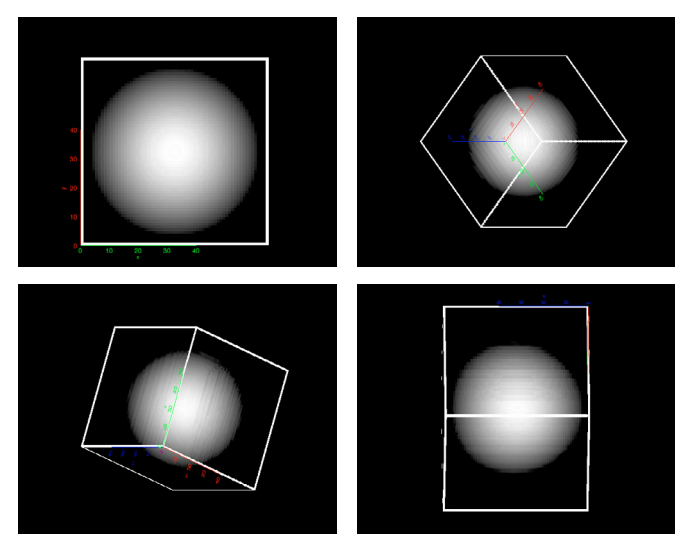


Fig. 14. Visualization of the results for the LTE case. The voxel grid has 65^3 elements. The intensity image is shown for $(\theta, \phi) = (0, 0)$ (*upper left panel*), (45, 45) (*bottom right panel*), (140, 250) (*upper right panel*), and (89, 139) (*bottom right panel*) degrees. The intensities are mapped linearly to 255 shades of gray. The direction of the axes are given with axes lengths corresponding to a total of 50 voxels. The borders of the front faces of the voxel cube are shown, their widths corresponds to the apparent width of a voxel. Note that the different panels are at different scales.

converges *more slowly* than the 32^2 and 64^2 grids. The higher resolution grids convergence rate compares well with the 1D code. This highlights the importance of the non-local Λ^* operator and a large enough solid angle grid for rapid convergence and accuracy.

3.2.3. Visualization

We have implemented a simple visualization of the results in order to view images of the emitted intensities. The visualization uses IDL to read the results of the 3D RT code, performs a formal solution for a specific (θ, ϕ) and displays the result as an image of the intensities leaving the voxel grid. These figures are extremely helpful for discovering even small problems with the generation and handling of the characteristics or issues due to low resolution in solid angle or space. Such problems will immediately show up as asymmetries in the generated images. We show the results for the LTE test (with 65³ voxels) in Fig. 14. The limb darkening of the test sphere is clearly visible in the figures. The slight pixellation and asymmetries are due to spatial and angular resolution. Note that the scales of the different panels are different due to the changing orientation of the data cube. The generated images for the $\epsilon = 10^{-4}$ test case with 129³ and 193³ voxels are shown in Figs. 15 and 16, respectively. For both figures, the source functions were calculated with 64² angles. The images show much less pixellation and far less artifacts than the images shown in Fig. 14. The results for the $\epsilon = 10^{-8}$ test case are shown in Fig. 17, they look similar to the $\epsilon = 10^{-4}$ case with the same grid sizes.

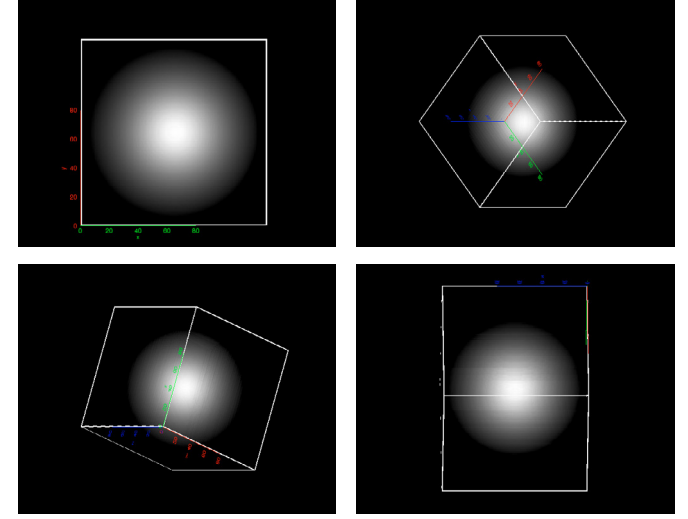


Fig. 15. Visualization of the results for the $\epsilon=10^{-4}$ case with a 129^3 elements voxel grid. The intensity image is shown for $(\theta,\phi)=(0,0)$ (upper left panel), (45,45) (bottom right panel), (140,250) (upper right panel), and (89,139) (bottom right panel) degrees. The intensities are mapped linearly to 255 shades of gray. The direction of the axes are given with axes lengths corresponding to a total of 100 voxels. The borders of the front faces of the voxel cube are shown, their widths corresponds to the apparent width of a voxel. Note that the different panels are at different scales.

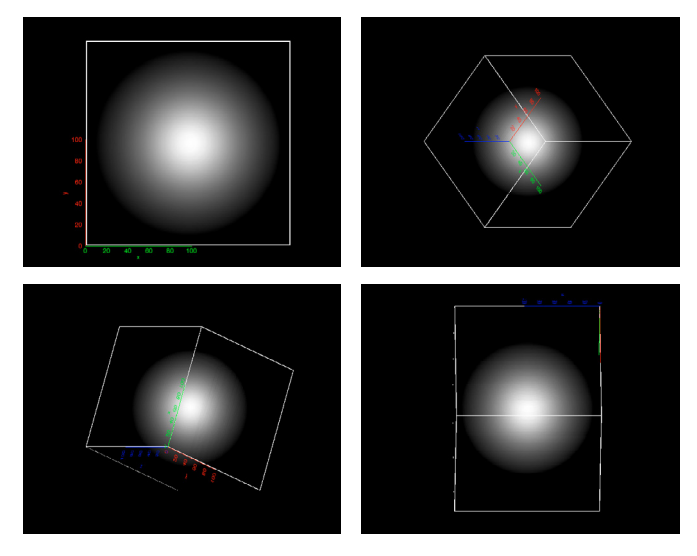


Fig. 16. Visualization of the results for the $\epsilon=10^{-4}$ case with a 193^3 voxel grid. The intensity image is shown for $(\theta,\phi)=(0,0)$ (upper left panel), (45,45) (bottom right panel), (140,250) (upper right panel), and (89,139) (bottom right panel) degrees. The intensities are mapped linearly to 255 shades of gray. The direction of the axes are given with axes lengths corresponding to a total of 100 voxels. The borders of the front faces of the voxel cube are shown, their widths corresponds to the apparent width of a voxel. Note that the different panels are at different scales.

3.2.4. MPI scaling properties

Figure 18 shows the scaling properties of the MPI version of the 3D radiation transport code for the $\epsilon=10^{-8}$ test case. The runs were performed on 2 parallel compute clusters,

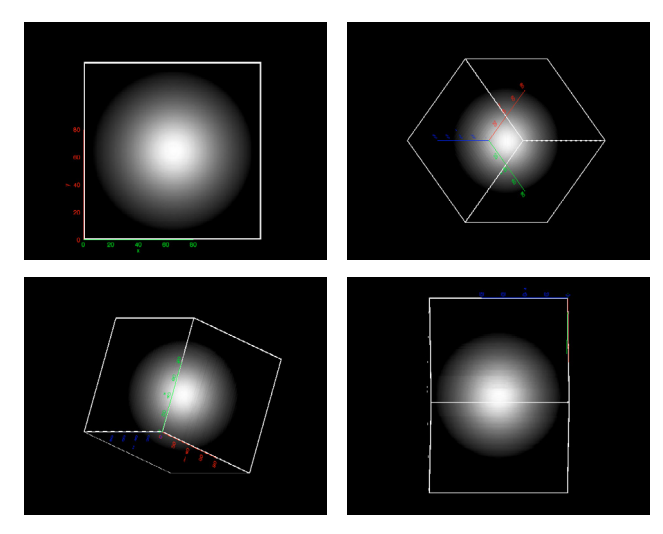


Fig. 17. Visualization of the results for the $\epsilon=10^{-8}$ case with a 129^3 elements voxel grid. The intensity image is shown for $(\theta,\phi)=(0,0)$ (upper left panel), (45,45) (bottom right panel), (140,250) (upper right panel), and (89,139) (bottom right panel) degrees. The intensities are mapped linearly to 255 shades of gray. The direction of the axes are given with axes lengths corresponding to a total of 100 voxels. The borders of the front faces of the voxel cube are shown, their widths corresponds to the apparent width of a voxel. Note that the different panels are at different scales.

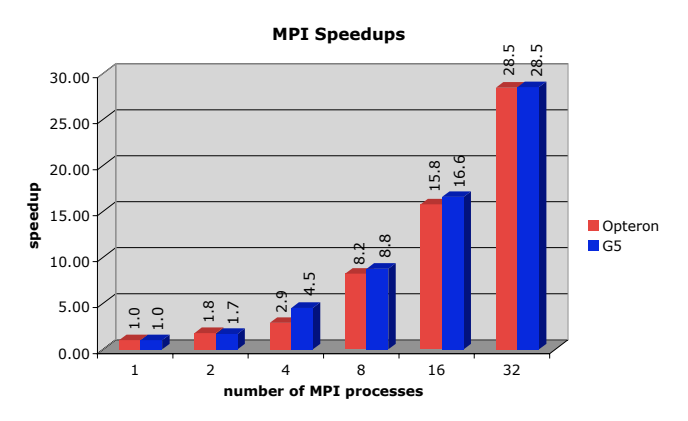


Fig. 18. Scaling properties of the MPI version of the 3D RT code for parallel clusters based on Opterons and G5 CPUs. In absolute scales the G5s are about 30% faster than the Opterons.

one equipped with 1.8 GHz dual Opteron CPUs and an Infiniband interconnect from Delta computer and one equipped with 2.0 GHz dual G5 CPUs with Gbit ethernet network from Apple computer (Xserves). The speedup we obtain in the MPI version is close to optimal, about a factor of 28 with 32 MPI processes on 32 CPUs (or 16 compute nodes). The fact that the speedup is very good shows that the load balancing is optimal and that the time spent in the MPI communication routines is negligible compared to the compute times.

With 129^3 voxels, the code uses about 0.6GB of memory. With 10 CPUs and 64^2 angles, the wallclock time for a formal solution is about 310s (400s) on 2.0 GHz Xserve G5s (on 1.8GHz Opterons), 9s (9s) for the required MPI communication, and between 3–26s (12–120s) to solve the linear system. Since the linear system is solved iteratively, the time

for the solution is reduces as the overall convergence limit is approached.

4. Conclusions

We have described a framework for solving three-dimensional radiative transfer problems in scattering dominated environments. The method uses a non-local operator splitting technique to solve the scattering problem. The formal solution is based on a long characteristic piece-wise parabolic procedure. For strongly scattering dominated test cases (sphere in a box) we find good convergence with non-local Λ^* operators, as well as minimal numerical diffusion with the long characteristics method and adequate resolution. A simple MPI parallelization gives excellent speedups on parallel clusters. In subsequent work we will implement a domain decomposition method to allow much larger spatial grids. Presently, we have implemented the method for static media, it can be used without significant changes to solve problems in the Eulerian-frame for media with low velocity fields. The distribution of matter over the voxels is, in the general 3D case, arbitrary. We chose a spherical test case to be able to compare the results our 1D code.

In Figs. 19 and 20 we compare the results for the $\epsilon=10^{-4}$ test case using a simple implementation of the short characteristics method and the long characteristics method used in this paper. The test grid contains 129^3 voxel and 64^2 angular points. The high diffusivity of the SC method is evident. Other authors (Steiner 1991; Fabiani Bendicho et al. 1997; Trujillo Bueno & Fabiani Bendicho 1995; Vath 1994; Auer et al. 1994; van Noort et al. 2002) have used SC methods in multi-dimensional radiative transport problems. Short characteristics techniques are faster but require special considerations to reduce numerical diffusion (Auer 2003). We may further look into the SC method in later papers.

We have generalized the operator splitting to include larger bandwidth operators. They lead to faster convergence although they do require more memory and ultimately more computing time. Nevertheless, they will be useful for highly complex problems and we have developed a highly flexible approach to the construction of the Λ^{\ast} operator so that the bandwidth may be set for each spatial point individually as the problem and computational resources require.

We have designed an especially general and flexible framework for 3D radiative transfer problems with scattering. In future papers of this series we will describe its extension to line transfer problems, multi-level NLTE calculations, and differentially moving flows.

Acknowledgements. This work was supported in part by by NASA grants NAG5-12127 and NAG5-3505, NSF grants AST-0204771 and AST-0307323. PHH was supported in part by the Pôle Scientifique de Modélisation Numérique at ENS-Lyon. Some of the calculations presented here were performed at the National Energy Research Supercomputer Center (NERSC), which is supported by the Office of Science of the U.S. Department of Energy under Contract No. DE-AC03-76SF00098; at the Höchstleistungs Rechenzentrum Nord (HLRN); and at the Hamburger Sternwarte Apple G5 and Delta Opteron clusters financially supported by the DFG and the State of

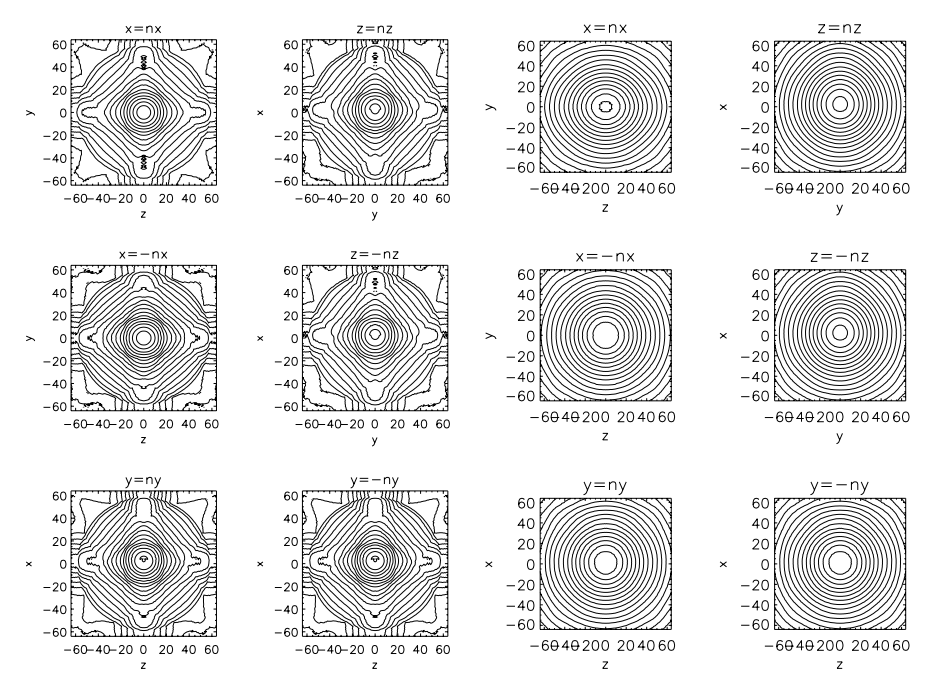


Fig. 19. Comparison of the mean intensity contour plots for the test case with $\epsilon = 10^{-4}$ with 129^3 spatial points and 64^2 solid angle points. The left panel shows the results obtained with the short characteristics method whereas the right panel shows the results of the long characteristics method. The axes are labeled by voxel index with (x, y, z) = (0, 0, 0) being the center of the voxel grid. Each plot shows one outside face of the voxel cube (the physical scales are the same an all directions).

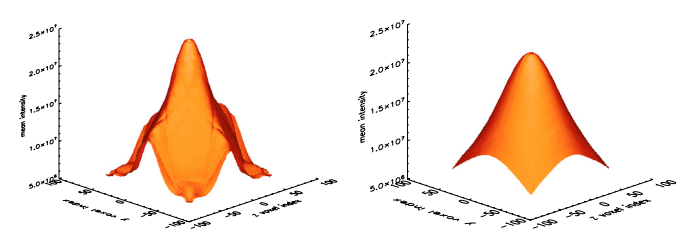


Fig. 20. Comparison of the mean intensity surfaces at the z-y face for the test case with $\epsilon=10^{-4}$ with 129^3 spatial points and 64^2 solid angle points. The left panel shows the results obtained with the short characteristics methods whereas the right panel shows the results of the long characteristics method. The axes are labeled by voxel index with (x, y, z) = (0, 0, 0) being the center of the voxel grid. Each plot shows one outside face of the voxel cube (the physical scales are the same in all directions).

Hamburg. We thank all these institutions for a generous allocation of computer time.

References

Adam, J. 1990, A&A, 240, 541

Anderson, E., Bai, Z., Bischof, C., et al. 1992, LAPACK Users' Guide (SIAM)

Auer, L. 2003, in Stellar Atmosphere Modeling, ed. I. Hubeny, D. Mihalas, & K. Werner (San Franscisco: ASP Conf. Series), 288 3

Auer, L., Fabiani Bendicho, P., & Trujillo Bueno, J. 1994, A&A, 292,

Cannon, C. J. 1973, JQSRT, 13, 627

Dykema, P. G., Klein, R. I., & Castor, J. I. 1996, ApJ, 457, 892
Fabiani Bendicho, P., Trujillo Bueno, J., & Auer, L. 1997, A&A, 324, 161

Golub, G. H., & Van Loan, C. F. 1989, Matrix computations (Baltimore: Johns Hopkins University Press)

Hamann, W.-R. 1987, in Numerical Radiative Transfer, ed.W. Kalkofen (Cambridge University Press), 35

Hauschildt, P. H. 1992, JQSRT, 47, 433

Hauschildt, P. H., & Baron, E. 2004, A&A, 417, 317

Hauschildt, P. H., Störzer, H., & Baron, E. 1994, JQSRT, 51, 875

Hummel, W. 1994a, Ap&SS, 216, 87

Hummel, W. 1994b, A&A, 289, 458

Hummel, W., & Dachs, J. 1992, A&A, 262, L17

Mihalas, D. 1978, Stellar Atmospheres (New York: W. H. Freeman)

Mihalas, D. 1980, ApJ, 237, 574

Mihalas, D., Kunasz, P., & Hummer, D. 1975, ApJ, 202, 465

Ng, K. C. 1974, J. Chem. Phys., 61, 2680

Norman, M. L. 2000, in Rev. Mex. Astron. Astrofis. Conf. Ser., 9, 66 Olson, G. L., & Kunasz, P. B. 1987, JQSRT, 38, 325

Olson, G. L., Auer, L. H., & Buchler, J. R. 1987, JQSRT, 38, 431 Papkalla, R. 1995, A&A, 295, 551

Rijkhorst, E.-J., Plewa, T., Dubey, A., & Mellema, G. 2005, A&A, in press [arXiv:astro-ph/0505213]

Steiner, O. 1991, A&A, 242, 290

Trujillo Bueno, J., & Fabiani Bendicho, P. 1995, ApJ, 455, 646 Turek, S. 1993, preprint

van Noort, M., Hubeny, I., & Lanz, T. 2002, ApJ, 568, 1066

Vath, H. M. 1994, A&A, 284, 319

Xiaoye, S. L., & Demmel, J. W. 2003, ACM Transaction on Mathematical Software, 29, 110

Zurmühl, R., & Falk, S. 1986, Matrizen und ihre Anwendungen, 5th ed., Vol. 2 (Berlin: Springer-Verlag)